

Polarization-Resolved p-Se/n-WS₂ Heterojunctions toward Application in Microcomputer System as Multivalued Signal Trigger

Ling Li, Ge Gao, Xueting Liu, Yiming Sun, Jianpeng Lei, Zecheng Chen, Zhiying Dan, Wei Gao, Tao Zheng, Xiaozhou Wang, Nengjie Huo,* and Jingbo Li*

Polarization-sensitive photodetectors based on van der Waals heterojunctions (vdWH) have excellent polarization-resolved optoelectronic properties that can enable the applications in polarized light identification and imaging. With the development of optical microcomputer control systems (OMCS), it is crucial and energy efficient to adopt the self-powered and polarization-resolved signal-generators to optimize the circuit design of OMCS. In this work, the selenium (Se) flakes with in-plane anisotropy and p-type character are grown and incorporated with n-type tungsten disulfide (WS₂) to construct the type-II vdWH for polarization-sensitive and self-powered photodetectors. Under 405 nm monochrome laser with 1.33 mW cm⁻² power density, the photovoltaic device exhibits superior photodetection performance with the photoelectric conversion efficiency (PCE) of 3.6%, the responsivity (*R*) of 196 mA W⁻¹ and the external quantum efficiency (EQE) of about 60%. The strong in-plane anisotropy of Se crystal structure gives rise to the capability of polarized light detection with anisotropic photocurrent ratio of ≈ 2.2 under the 405 nm laser (13.71 mW cm⁻²). Benefiting from the well polarization-sensitive and photovoltaic properties, the p-Se/n-WS₂ vdWH is successfully applied in the OMCS as multivalued signal trigger. This work develops the new anisotropic vdWH and demonstrates its feasibility for applications in logic circuits and control systems.

ratio and wide applications in polarized light imaging, target tracking, and remote sensing.^[1,2] Recently, van der Waals materials with in-plane anisotropic structures such as tungsten telluride (WTe₂), germanium arsenic (GeAs), and gallium arsenide (GaAs), have emerged as a promising optical medium to realize high-performance polarization-resolved photodetectors.^[3–7] Through the construction of van der Waals heterojunctions (vdWH) composed of anisotropic materials such as Te/MoSe₂ and BP/WSe₂, the type-II band alignment or built-in electric field at p–n interface can result in the self-powered and polarization-sensitive photodetections.^[8–10]

Optical microcomputer control systems (OMCS) are widely applied in our lives, such as space exploration, distance measurement, and positioning systems.^[11–13] However, the general photodetector acting as a signal generator in the OMCS can merely obtain light intensity information and require an external power supply, which can increase the complexity and

instability of circuit design, limiting the wide applications with low-power consumption. Therefore, the vdWH-based polarization-sensitive photodetectors can fulfill the low-power requirement of the current OMCS, severing as a self-powered and polarization-dependent signal generator, which can increase the number of logic states to trigger OMCS by identifying the light polarization information.

In this work, we have grown the selenium (Se) flakes with in-plane anisotropy and p-type character and fabricated the p-Se/n-WS₂ vdWH-based polarized light detectors that have been applied in a microcontroller for the first time. Under 405 nm monochrome laser with 1.33 mW cm⁻² power density, in the heterojunctions, the photoelectric conversion efficiency (PCE) reaches 3.6% and the external quantum efficiency (EQE) is 60%. Thanks to the polarization properties of Se, the vdWH devices exhibit the anisotropic photocurrent ratio of ≈ 2.2 under the 405 nm laser (13.71 mW cm⁻²). Taking advantage of the high on–off ratio and polarization sensitivity, we apply the device in OMCS, opening up new application scenarios in integrated circuit using the next generation of anisotropic van der Waals heterojunctions.

1. Introduction

Polarization-sensitive photodetectors can extract the information of power intensity, wavelength, and polarization direction from the incident light, enabling a higher signal-to-noise

L. Li, G. Gao, X. Liu, Y. Sun, Z. Chen, Z. Dan, W. Gao, T. Zheng, X. Wang, N. Huo, J. Li

Institute of Semiconductors
South China Normal University
Guangzhou 510631, P. R. China
E-mail: njhuo@m.scnu.edu.cn; jbli@semi.ac.cn

J. Lei
Nanchang Hangkong University
Nanchang 330036, P. R. China

J. Li
Guangdong Provincial Key Laboratory of Chip
and Integration Technology
Guangzhou 510631, P. R. China

The ORCID identification number(s) for the author(s) of this article can be found under <https://doi.org/10.1002/smll.202202523>.

DOI: 10.1002/smll.202202523

2. Results and Discussion

The Se flakes are grown by physical vapor deposition (PVD) method, and the details can be seen in the experimental section. From the atomic structure as shown in Figure 1a, the 2D Se layers exhibit anisotropic in-plane lattice structure with a 1D chain along the direction of *b*-axis [0001].^[1] The few-layer WS₂ is mechanically exfoliated from the WS₂ crystal. Then, the Se/WS₂ heterojunctions can be obtained by the dry-transfer method. The Ti/Au (5/50 nm) electrodes are fabricated by UV lithography and electron beam evaporation techniques. The schematic diagram and optical microscopy image of the Se/WS₂ heterojunction device are shown in Figure 1b and Figure S1 (Supporting Information), respectively. Figure 1c shows the Raman vibration modes of both WS₂ and Se as well as the overlapping region, exhibiting the typical Raman peaks of WS₂ and Se.^[1,14] As shown in Figure S2 (Supporting Information), there are two degenerate E-modes of the in-plane phonon vibration mode in Se, which are separated into bond bending (E_{1g}) and bond stretching (E_{2g}) types. The E_{1g} mode located at 144 cm⁻¹ is caused by the *a*-axis rotation, and the E_{2g} mode at 233 cm⁻¹ is mainly an asymmetric stretch along the *b*-axis direction, which makes the E_{2g} mode appear anisotropic in the angle-resolved polarized Raman (ARPR) measurements.^[15,16] From the atomic-force microscopy (AFM) height profiles as shown in Figure 1d, the thickness of WS₂ and Se in heterojunctions are 40 and 33 nm, respectively.

To identify the band alignment of Se/WS₂ heterojunctions, the band structure and density state diagrams of Se and WS₂ are obtained using the first-principles calculation. As shown in Figure S3 (Supporting Information), the conduction band minimum (CBM) and valence band maximum (VBM) of Se are occupied by Se-*p* orbitals, which are located at the H and L points of the Brillouin zone, respectively, leading to the indirect bandgap of ≈2.05 eV. For multilayer WS₂, the CBM and VBM are dominated by the W-*d* state with indirect bandgap of

≈1.59 eV. Kelvin probe force microscopy (KPFM) can be used to measure the in situ surface potential difference (SPD) between material and KPFM tip, which can be calculated using the formula $V_{SPD} = (W_{tip} - W_{sample})/q$,^[17] where *q* is the elementary charge, *W*_{tip} and *W*_{sample} are the work function of tip and the sample, respectively. As shown in Figure 1e, the SPD between Se and WS₂ is about 124 mV, corresponding to the work function or Fermi level difference of 124 meV.^[18] The SPD images at the lateral interface of Se/WS₂ heterojunctions visually demonstrate the potential difference (Figure S4, Supporting Information). The surface potential of Se is higher than that of WS₂, indicating the larger work function of Se, the electrons in WS₂ can transfer to Se side, reaching an equilibrium state with large built-in electric field. Besides, from the transfer curves of individual Se and WS₂ transistors, they exhibit p-type and n-type behaviors, respectively (Figure S5, Supporting Information). According to the above theoretical and experiment results, we can plot the diagram of band alignment before and after contact as shown in Figure 1f. The Se/WS₂ heterojunction forms a type II band alignment and well p-n interface after contact, the subsequent charge transfer can lead to the band bending and built-in electric field at interface, providing a photovoltaic effect in the device.

Now we turn to the photoelectric properties of Se/WS₂ heterojunction device. During the photoelectric measurement, the 405 nm laser with a spot size of 1 mm was used. The laser power intensity in the spot center and the edge is essentially uniform, with no significant Gaussian distribution. We first measure the total power of the incident laser and then calculate the power density by dividing the total power over the spot area. Thus, the photoelectric parameters are calculated based on the laser power density obtained above. Figure 2a shows the *I*-*V* curve of Se/WS₂ device, exhibiting the diode behavior with a current rectification ratio (CR) of 443. The CR can be obtained by the formula: $CR = I_{V+} + I_{V-}$, where *I*_{V+} and *I*_{V-} represent the operating current of the device at an equal size bias but in the opposite direction, respectively.^[19] The ideal factor

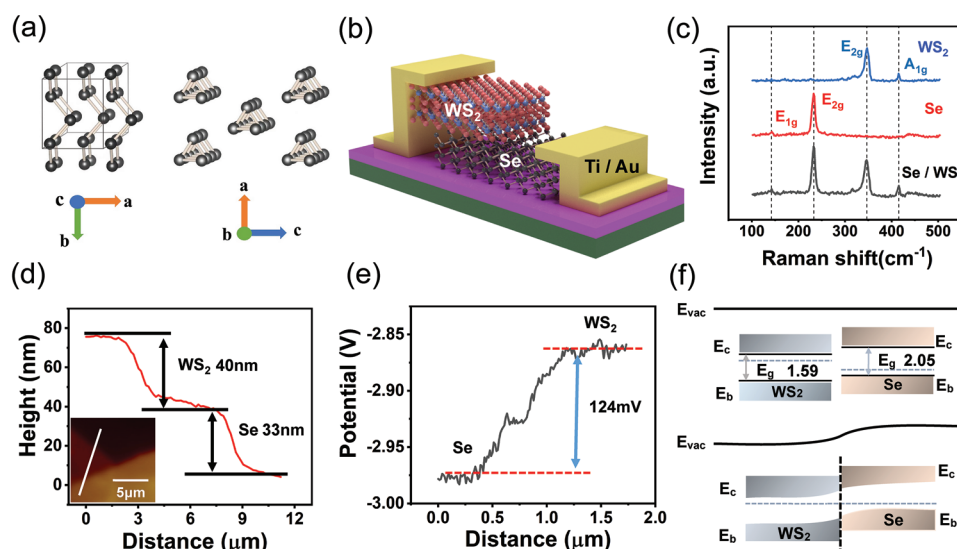


Figure 1. Characterization of Se/WS₂ heterojunction device. a) Atomic structure diagram of selenium. b) Schematic diagram of the Se/WS₂ device. c) Raman spectra of Se, WS₂, and overlapping region. d) AFM image of the Se and WS₂. e) In situ surface potential difference (SPD) plot of the measured Se/WS₂ interface. f) Band diagram of the Se/WS₂ heterojunction forming a type II band arrangement.

(n) is calculated to be ≈ 1 in the range of V_{sd} of 0–0.3 V, using the formula: $n = \frac{q}{k_b T} \frac{dV}{d \ln I}$, where q , k_b , and T are elementary charge, Boltzmann constant and Kelvin temperature,^[20] indicating the dominated diffusion current due to the high quality of the heterojunction with no recombination centers caused by defects. Figure 2b and Figure S6 (Supporting Information) illustrate the logarithmic and linear scale I – V characteristics of Se/WS₂ device under 405 nm laser illuminations with different powers, respectively. The device exhibits significant photovoltaic properties with large open circuit voltage (V_{oc}) and short circuit current (I_{sc}). Both V_{oc} and I_{sc} as function of light power density are plotted as shown in Figure 2c, reaching 0.4 V and 7.5 nA, respectively, at 35.73 mW cm^{−2}. The electrical power (P_{el}) as function of V_{sd} under various light power is shown in Figure 2d. The photoelectric conversion efficiency (PCE) is an important parameter of solar cells, and the formula is $PCE = P_{el} \max / P_{in \text{ laser}}$. Thus, the PCE of Se/WS₂ device can reach 3.6% at 1.33 mW cm^{−2}, as shown in Figure 2e, indicating the potential energy-harvesting applications.

At a bias of 0 V, we measured the dynamic photoresponse under different light power densities shown in Figure 2f, implying self-driven and fast response. Figures S7 and S8

(Supporting Information) exhibit the temporal response under various excitation power density, exhibiting the rise and decay time on the order of 30–80 ms. The photocurrent ($I_{ph} = I_{light} - I_{dark}$) as function of laser power can be well fitted by the power-law formula $I_{ph} \sim P_l^\vartheta$, where ϑ is the fitting index, P_l is the laser power. The ϑ reaches 0.83 from the fitting curves (Figure 2g), indicating the less defect recombination centers at heterojunction interface.^[21] With the increased laser power, the photo-switching ratio can reach 1.9×10^4 under 35.73 mW cm^{−2} laser power, showing the high logic swing characteristics. The responsivity (R) and external quantum efficiency (EQE) can be calculated with the formula $R = \frac{I_{ph}}{P_l}$ and $EQE = \frac{hcR}{q\lambda}$, respectively,

where λ is the wavelength of incident light, q is the electronic charge, h is the Planck constant, and c is the light velocity. The maximum R and EQE are 0.196 A W^{−1} and 60% under the 1.33 mW cm^{−2} laser power, respectively (Figure 2h). With the increase of laser power, the scattering effect and the recombination rate increase, so that R and EQE decrease.^[22,23] The detectivity (D^*) is used to clarify the minimum detection signal of the photodetector, and can be evaluated with the formula $D^* = \frac{RS^{0.5}}{(2qI_d)^{0.5}}$, where R is the responsivity, S is overlapping

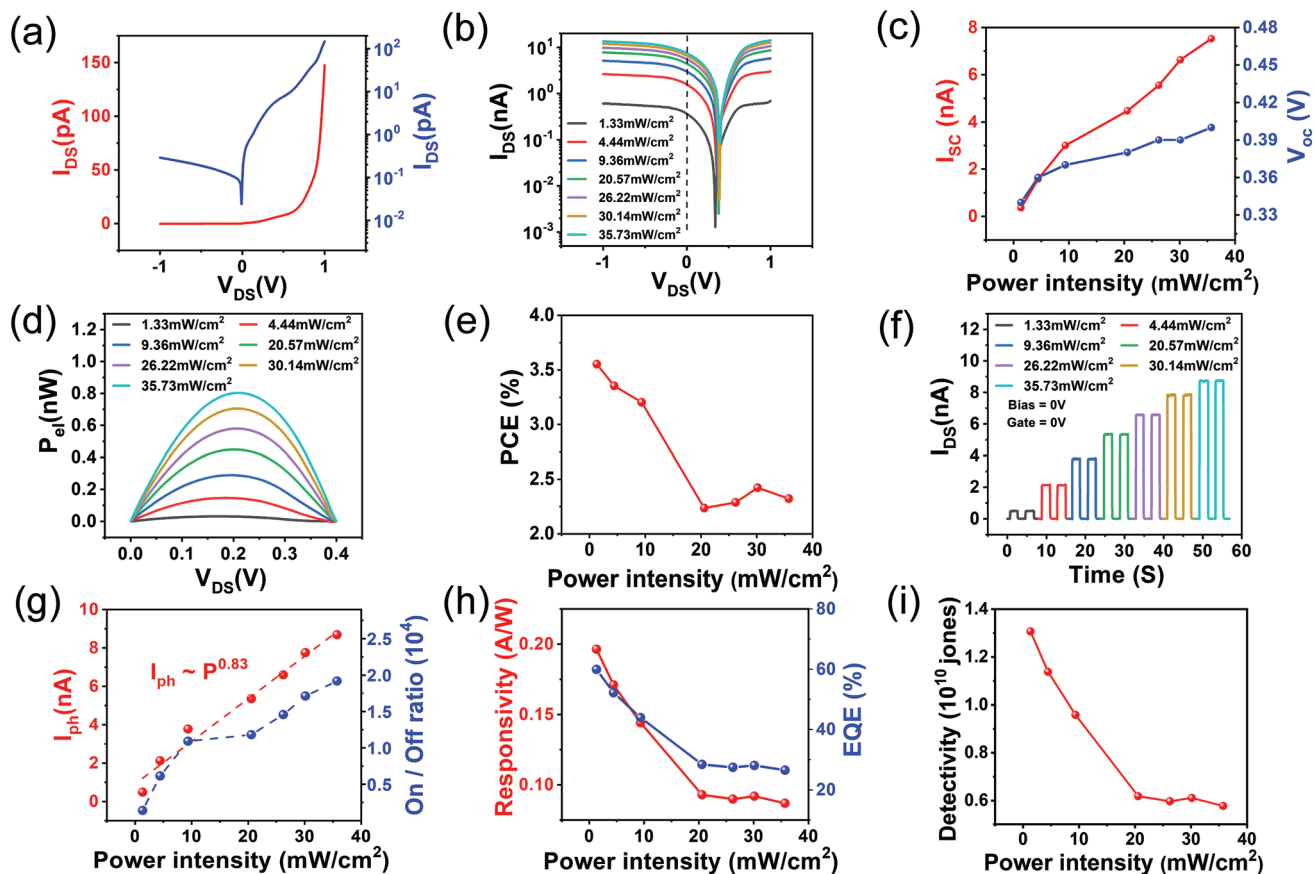


Figure 2. Photovoltaic and photodetection characteristics of Se/WS₂ heterojunction device. a) I – V characteristics of Se/WS₂ heterojunction device. b) Logarithmic scale I – V characteristics under different 405 nm laser power intensity. c) Short-circuit current and open-circuit voltage as a function of 405 nm laser power intensity. d) Electrical power (P_{el}) – V_{sd} characteristics under different laser power intensity. e) Photoelectric conversion efficiency as a function of laser power intensity. f) Dynamic photoresponse under different laser power intensity. g–i) I_{ph} and on/off ratio, responsivity and external quantum efficiency, detectivity as a function of 405 nm laser power intensity.

Table 1. Comparison of the device performances among different 2D material-based photodetectors.

Material	Wavelength [nm]	Open circuit voltage [V]	Short circuit current [nA]	Photo switching ratio	Detectivity [D^*] [Jones]	Refs.
Se/WS ₂	405	0.4	7.5	1.98×10^4	1.3×10^{10}	This work
Te/Si	405	0.28	2	—	1×10^{13}	[30]
WSe ₂ /Bi ₂ Te ₃	633	0.25	18	1.8×10^4	—	[31]
Gr/Si	850	—	—	1×10^4	1.4×10^8	[32]
WSe ₂ -WSe ₂ homojunction	532	0.44	0.1	—	4.4×10^{10}	[24]
WSe ₂ p-n junction	470	—	—	1×10^3	6.18×10^8	[33]

region between WS₂ and Se, I_d is the dark current. The D^* is calculated to be 1.3×10^{10} Jones under low light power (Figure 2i), which is better than that in the reported van der Waals heterojunction.^[24–28] The fill factor (FF) of the device can be calculated by the formula $FF = \frac{P_{elmax}}{V_{oc} \cdot I_{sc}}$, where V_{oc} is the open circuit voltage, I_{sc} is the short circuit current, and P_{elmax} is the maximum value of the electrical power.^[29] Figure S9 (Supporting Information) shows the FF as a function of the laser power density, the FF increases with increased laser power and can reach the maximum value of 26.8% at 26.22 mW cm⁻². The stability test was also performed by switching the laser on/off periodically (Figure S10, Supporting Information), illustrating the high stability of photoresponse after hundreds of cycles. **Table 1** compares the device performance with that in the previously reported 2D material-based photodetectors, implying the superior photovoltaic and photodetection performance of our heterojunction devices.^[24,30–33]

Polarization-sensitive photoresponse is a new degree of freedom for extracting the polarization information of light, enabling the photodetection and imaging with higher contrast in a complex environment.^[8,34] The prerequisite to realize the polarized light detection is the anisotropic crystal structure and photoabsorption in low-symmetric van der Waals materials such as GeSe, BP, p-Te, ReS₂, and so on.^[8,35–37] In our case, we performed the angle-resolved polarized Raman (ARPR) measurements for the PVD-grown Se flakes. The ARPR was performed using a Raman measurement instrument (Nost Technology Co., Ltd) with a 532 nm laser. The polarization angle changes by rotating the sample in 10° steps. **Figure 3a,b** shows the polar and mapping plots of ARPR intensities in parallel and cross configurations, respectively. Under different configurations, the polarized Raman plots of few layers Se exhibit different polarization properties, which indicates the diversity of polarized Raman modes and the lower symmetry of its crystal structure. In the parallel configuration, the polarized Raman plot exhibits a two-leaf clover shape with a period of 180°, and its data can be fitted by the formula $b(\theta) = b_{max}\sin^2(\theta + \varphi) + b_{min}\cos^2(\theta + \varphi)$, where θ is the angle of the linearly polarized laser, b_{min} and b_{max} are the minimum and maximum fitting parameters, respectively. In the cross configuration, the Raman plot exhibits a four-leaf clover shape with a period of 180°, and the data can be well fitted by the formula $I(E_{2g}) \propto (\cos^2(\theta) + a/b \cdot \sin^2(\theta) \cdot \cos(\varphi_{ab}))^2 + \sin^2(\theta) \sin^2(\varphi_{ab})$, where θ is the angle of the linearly polarized laser, a , b are the minimum and maximum fitting parameters, respectively.

Now, we focus on the polarization-sensitive characteristics of photocurrent in Se/WS₂ heterojunction-based device. The circularly polarized laser (405 nm, 26.22 mW cm⁻²) passes through a polarizer to form a linearly polarized laser. The polarization angle varies with the rotation of the polarizer from 0 to 360° (30° steps). **Figure 3c** shows the time-dependent photocurrent by varying the polarization angles at zero bias while keeping the light power same. We extract the photocurrent as function of polarization angle in polar plot as shown in **Figure 3d**. When the polarizer is at 0°, the b -axis of the Se and the polarized laser is parallel (Se atomic structure diagram is shown in **Figure 1a**). With the rotation of the polarizer, the photocurrent reaches its maximum and minimum values at 90° and 0° of polarized light, respectively. The experimental data can be fitted by the formula $c(\theta) = c_{min}\sin^2(\theta\varphi) + c_{max}\cos^2(\theta + \varphi)$, where θ is the angle of the linearly polarized laser, c_{min} and c_{max} are the minimum and maximum fitting parameters, respectively. The polarization ratio (defined as I_{max}/I_{min}) is calculated to be 1.78, which is comparable to the polarized heterojunction device.^[38–40] It is worth noting that WS₂ exhibits the isotropic photocurrent and Raman intensity, which has also been measured as varying polarization angles (**Figures S11 and S12**, Supporting Information). Therefore, the polarization feature in the heterojunction device is dominated by Se component. **Figure 3e** shows the polarization ratio of photocurrent under different bias and gate voltages, which indicates that the polarization ratio can be regulated by both drain and gate voltage, reaching 2.2 at V_g of 40 V. The corresponding polar diagrams are shown in **Figure S13** (Supporting Information).

Taking advantage of high-performance, self-driven, and polarization-sensitive photodetections, we then exploit the Se/WS₂ vdWH device in application of the microcomputer control system, and its schematic diagram is shown in **Figure 4a**. In the setup, the Se/WS₂ device can convert laser signals into electrical signals, the electrical signal processing system (ESPS) can reduce the electronic noise and amplify the electrical signal, the single-chip microcomputer (SCM) executes the corresponding instructions according to the collected electrical signal. In order to establish the communication between the instructions and the electrical signal, we use Proteus and Multisim software to simulate and set the SCM to execute different instructions. The corresponding circuit diagram in Proteus and Multisim software is shown in **Figures S14 and S15** (Supporting Information). In order to clarify the application principle of the microcomputer control system, we use **Figure 4b** to illustrate signals transmission and processing in the microcomputer control system. In the experiment, the chopper can divide the

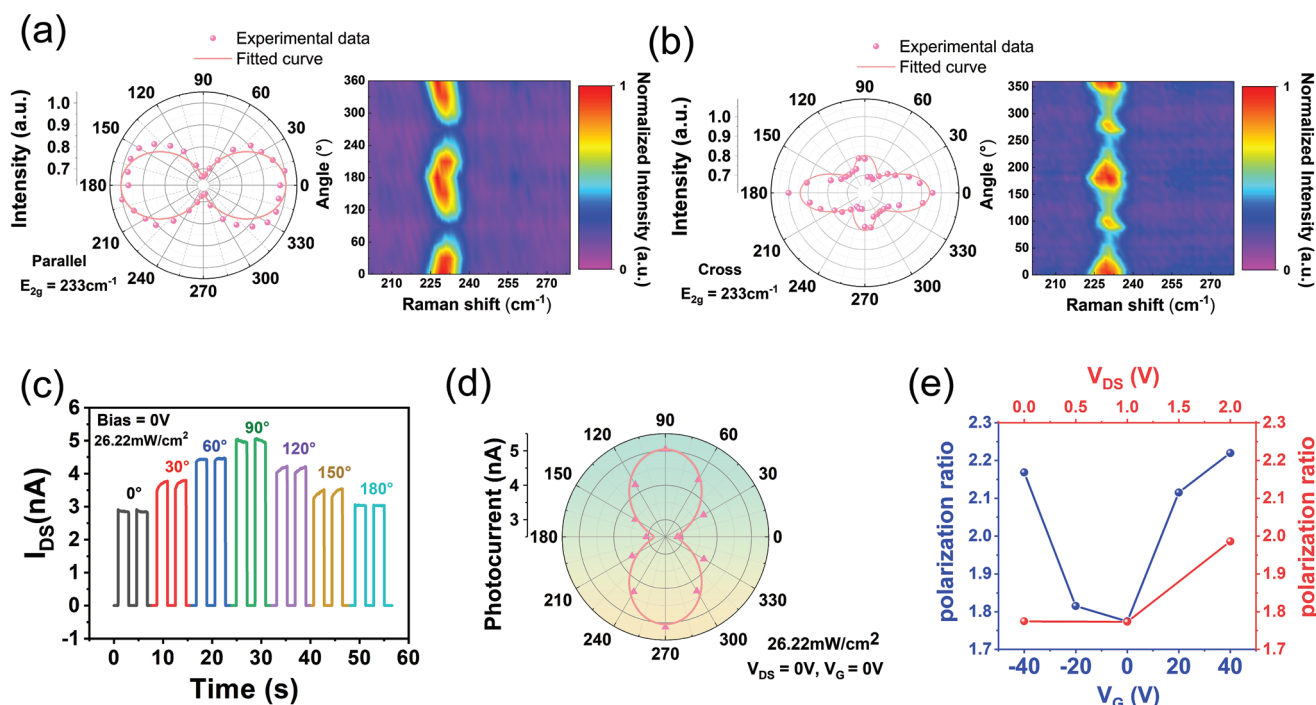


Figure 3. Polarization-resolved characteristics of the Se/WS₂ heterojunction device. Angle-resolved polarized Raman polar plot (E_{2g} mode intensity) and mapping plot of Se flakes in a) parallel and b) cross configuration (determining by the angle between incident laser and scattered light). c) Polarization-dependent self-powered current as a function of time and polarization angle under the 405 nm laser (26.22 mW cm⁻²) with switching on/off. d) Polar plot of photocurrent at different polarization angles. e) Polarization ratio under different bias and gate voltages.

laser into “off” and “on” states. At the “on” state, the photovoltaic characteristic of Se/WS₂ device can convert laser signal into the self-powered photocurrent. The ESPS can then smooth and amplify the photocurrent while maintaining the waveform. When the signal is acquired and transmitted to the SCM, it uses the threshold algorithm in the digital logic mode to identify the input signal. When the photocurrent is higher than the threshold current, the SCM recognizes it as logic state “1”; the dark current is recognized as logic state “0.” As shown in Figure 4c, the Se/WS₂ device outputs photocurrent (logic “1”) and dark current (logic “0”) to trigger the SCM. This shows that the self-powered signal output by the Se/WS₂ device can control the SCM. In the statistics of 200 cycles, the signal recognition rate is 97%, which can be attributed to the stable photoresponse and high logic swing in the Se/WS₂ device.

Under the excitation of polarized light, the amplitude of photocurrent periodically changes with the angle of the polarized laser. Subsequently, the polarization-resolved photocurrent can be recognized by the SCM as multiple logic states to execute different instructions. In Figure 3c, it is confirmed that the Se/WS₂ device can output a stable self-powered polarized photocurrent, acting as signal generator with multiple logic states to trigger the SCM. In order to improve the accuracy of signal recognition by SCM, the polarizer is rotated by 30° to switch different logic states. Figure 5a illustrates the transmission and processing procedures of polarization-resolved signals with multiple logic states in the microcomputer control system. It is noted that the same logic state is recognized by the microcontroller at x° (range 0–90°) and (180– x)°. Because the relationship

between polarization angles and photocurrent exhibits a double-lobe shape in the polar plot (Figure 3d). Therefore, we set up the calibration algorithm on SCM to distinguish these logic states, as shown in Figure 5b. The first signal transmitted from the device to the SCM is used as the calibration signal. When rotating the polarizer clockwise, the photocurrent intensity trends are opposite in the range of 0–90° (increased) and 90–180° (decrease). Therefore, we can use the second signal (effective signal) to compare with the calibration signal to distinguish the two polarization angles.

As shown in Figure 5c, when the polarization angle is rotated clockwise, the device can output 6 logic states to trigger the microcontroller, displaying the corresponding polarization angles on the screen. In addition, the number of LED lights on SCM is used to represent the polarization photocurrent intensity in different logic states, which increases with the polarized photocurrent intensity. The polarized photocurrent is minimum when the polarization angle is at 0°, and one LED light is on. The polarized photocurrent is maximum when the polarization angle is at 90°, and four LED light up. This indicates that the self-driven polarized photocurrent in the device has potential to drive the SCM to execute multivalued commands with low power consumption, such as adjusting the three-phase motor rotational speed and applying in the human–computer interaction system, etc. Figure S16 (Supporting Information) shows that when the polarization angle is rotated counterclockwise, the device can also trigger the microcontroller with similar functions. Note that when the polarizer is rotated counterclockwise, the change trend of polarization photocurrent intensity

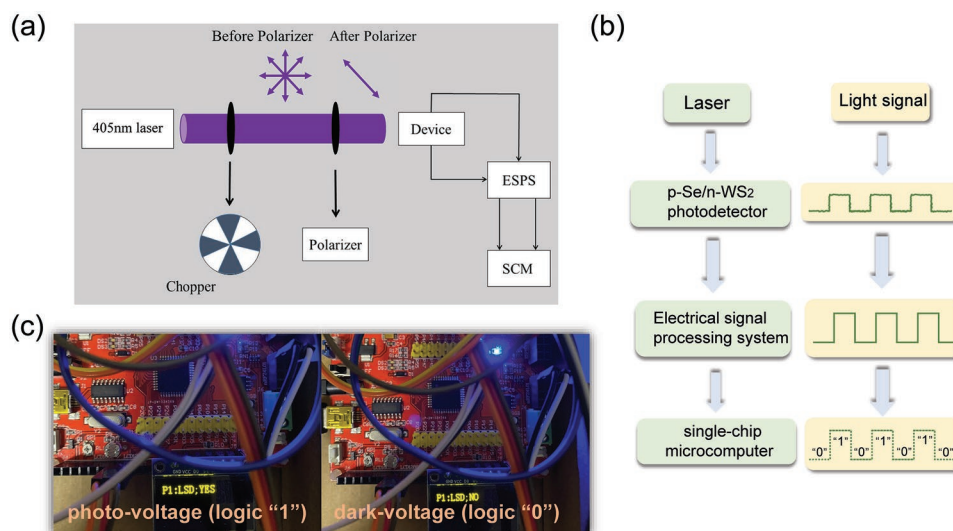


Figure 4. Application scheme in microcomputer control system using the photovoltaic properties of Se/WS₂ devices. a) Schematic diagram of OMCS based on Se/WS₂ device. b) Signals transmission and processing in the microcomputer control system. c) The Se/WS₂ device triggers the microcomputer control system in the dark and the laser is turned on.

is opposite to that in the clockwise rotation. Therefore, the calibration algorithm is different, which is switched through the button on the SCM. In the statistics of 50 cycles, the signal recognition rate is 34%. In the future research, we will improve the recognition rate of the multivalued signal by increasing the polarization ratio of the device and reducing the environmental noise.

3. Conclusion

In summary, the Se flakes with anisotropic structure and air stability have been grown with a scalable PVD method, then the Se/WS₂ vdWH were constructed as photovoltaic and polarization-resolved photodetectors due to the type-II band alignment and well p-n interface. In the self-driven mode under

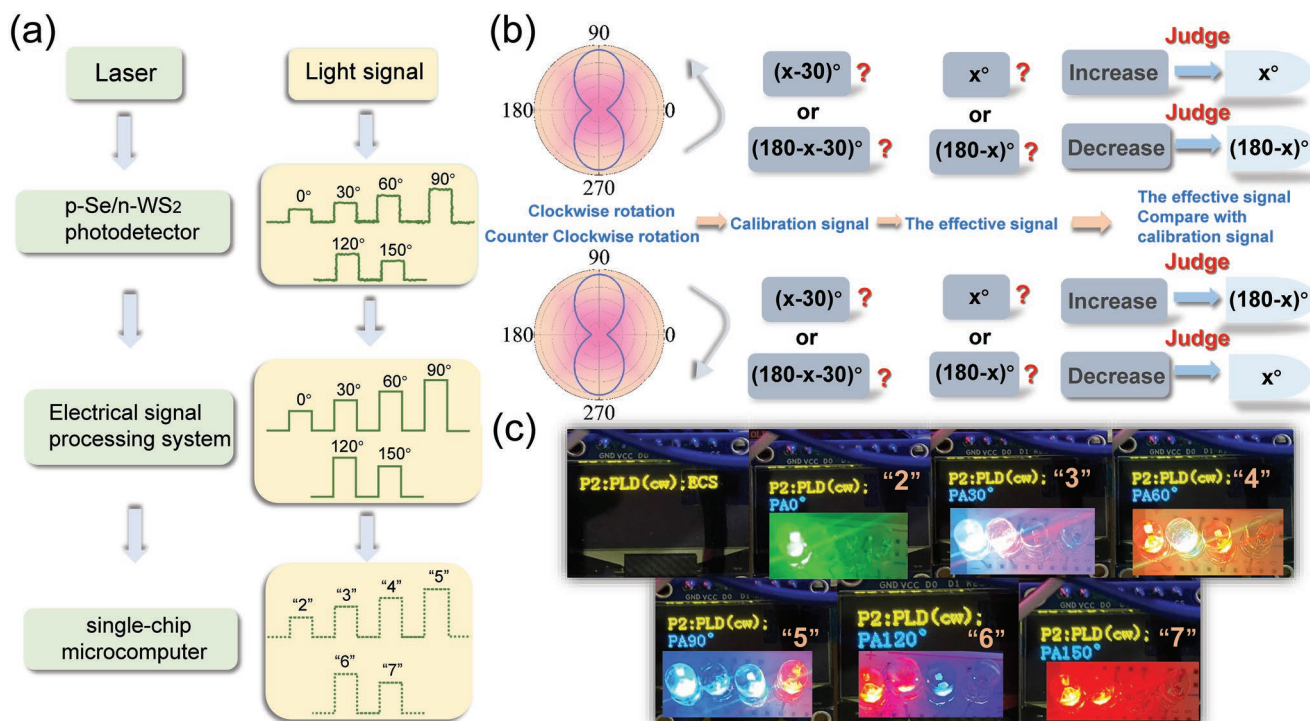


Figure 5. Application scheme in microcomputer control system using polarized photovoltaic properties of Se/WS₂ devices. a) Polarized signals transmission and processing in the microcomputer control system. b) Schematic diagram of the calibration algorithm on the microcontroller. c) When the polarization angle is rotated clockwise, the Se/WS₂ device triggers the microcomputer control system at different polarization angles.

the 405 nm laser, the devices exhibit high light switching ratio of 1.9×10^4 (35.73 mW cm^{-2}) and large gate modulated photocurrent polarization ratio of ≈ 2.2 (13.71 mW cm^{-2}). Benefiting from the high polarization-sensitive characters, the Se/WS₂ vdWH has been successfully applied in the microcomputer system as multivalued signal trigger. Through laser switching on/off, the device can output two logic states to trigger the SCM in digital logic mode. Utilizing the polarization-resolved photocurrent, six logic states can be outputted to trigger SCM in analog logic mode. Multivalued logic states are commonly used in systems such as space exploration and human–computer interaction system. Compared with traditional two logic states, multivalued logic states have more combinations and can control SCM to execute complex instructions. This work reports for the first time the prototype device based on van der Waals heterojunctions that can stably output multivalued logic states under zero bias, indicating that polarized photodetectors based on anisotropic vdWH have potential commercial application value in microcomputer system as multivalued signal trigger.

4. Experimental Section

VASP Settings: In the electronic energy band structure of the VASP program, the cutoff energy of Se and WS₂ plane wave extension are set to 400 eV. Geometry optimization was performed, relaxing both ions and lattices until the total energy variation was less than 10^{-5} eV. The lattice constants of the eight-layer WS₂ supercell are $a = b = 3.18147 \text{ \AA}$, $c = 71.8096 \text{ \AA}$, and the vacuum thickness is 15 Å to avoid the interlayer interaction induced by periodic boundary conditions. The lattice constants of Se flakes is $a = b = 4.57827 \text{ \AA}$, $c = 4.94945 \text{ \AA}$. The special k-grid for Se and WS₂ band structure calculation is generated by the line mode of VASP. The k-point grids for calculating the geometry optimization of the Se and WS₂ are $12 \times 12 \times 7$ and $15 \times 15 \times 1$, respectively.

PVD Growth Process of Se flakes: The quartz boat filled with 10 mg selenium powder (Macclin, 99.99%) was located in the center of the tube furnace (OTF-1200X-S), then the silicon substrate ($1 \text{ cm} \times 1 \text{ cm}$) was located in the downstream side and 15–18 cm away from the selenium powder. Before growth, the high pure N₂ was first flowed at 150 sccm for 5 min to remove air in the tube. During growth, the temperature of the tube furnace rises from room temperature for 20 min to 300 °C and holds for 180 min; the N₂ flow rate was set to be 50 sccm, the air pressure in the tube was 1atm.

Supporting Information

Supporting Information is available from the Wiley Online Library or from the author.

Acknowledgements

L.L., G.G., and X.L. contributed equally to this work. The authors acknowledge financial support from the National Natural Science Foundation of China (No. 11904108, 62004071), the China Postdoctoral Science Foundation (No.2020M672680), and “The Pearl River Talent Recruitment Program” (No. 2019ZT08X639).

Conflict of Interest

The authors declare no conflict of interest.

Data Availability Statement

The data that support the findings of this study are available from the corresponding author upon reasonable request.

Keywords

optical microcomputer control systems, polarization-sensitive photodetectors, Se/WS₂ heterojunction, self-powered photodetectors, type II band alignment

Received: April 23, 2022

Revised: July 7, 2022

Published online: July 29, 2022

- [1] J. Qin, G. Qiu, J. Jian, H. Zhou, L. Yang, A. Charnas, D. Y. Zemlyanov, C.-Y. Xu, X. Xu, W. Wu, H. Wang, P. D. Ye, *ACS Nano* **2017**, *11*, 10222.
- [2] L. C. Lentz, A. M. Kolpak, *J. Phys.: Condens. Matter* **2020**, *32*, 155901.
- [3] J. Xiong, Y. Sun, L. Wu, W. Wang, W. Gao, N. Huo, J. Li, *Adv. Opt. Mater.* **2021**, *9*, 2101017.
- [4] W. Zhou, J. Chen, H. Gao, T. Hu, S. Ruan, A. Stroppa, W. Ren, *Adv. Mater.* **2019**, *31*, 1804629.
- [5] C. Jia, D. Wu, E. Wu, J. Guo, Z. Zhao, Z. Shi, T. Xu, X. Huang, Y. Tian, X. Li, *J. Mater. Chem. C* **2019**, *7*, 3817.
- [6] J. Wang, S. Gudiksen Mark, X. Duan, Y. Cui, M. Lieber Charles, *Science* **2001**, *293*, 1455.
- [7] C. Soci, A. Zhang, B. Xiang, S. A. Dayeh, D. P. R. Aplin, J. Park, X. Y. Bao, Y. H. Lo, D. Wang, *Nano Lett.* **2007**, *7*, 1003.
- [8] Q. Zhao, F. Gao, H. Chen, W. Gao, M. Xia, Y. Pan, H. Shi, S. Su, X. Fang, J. Li, *Mater. Horiz.* **2021**, *8*, 3113.
- [9] L. Ye, P. Wang, W. Luo, F. Gong, L. Liao, T. Liu, L. Tong, J. Zang, J. Xu, W. Hu, *Nano Energy* **2017**, *37*, 53.
- [10] Y. Sun, J. Xiong, X. Wu, W. Gao, N. Huo, J. Li, *Nano Res.* **2022**, *15*, 5384.
- [11] C. Zhu, Y. Chen, Y. Du, Y. Zhuang, F. Liu, R. E. Gerald, J. Huang, *IEEE Sens. J.* **2017**, *17*, 5523.
- [12] T. A. Tameh, R. Kashyap, M. Sawan, *J. Lightwave Technol.* **2018**, *36*, 2000.
- [13] E. Fujiwara, L. E. da Silva, T. H. R. Marques, C. M. B. Cordeiro, *Opt. Eng.* **2018**, *57*, 116107.
- [14] Y. Zhao, S. Han, J. Zhang, L. Tong, *J. Raman Spectrosc.* **2021**, *52*, 525.
- [15] Y. Du, G. Qiu, Y. Wang, M. Si, X. Xu, W. Wu, P. D. Ye, *Nano Lett.* **2017**, *17*, 3965.
- [16] R. Martin, G. Lucovsky, K. Helliwell, *Phys. Rev. B* **1976**, *13*, 1383.
- [17] W. Ahmad, J. Liu, J. Jiang, Q. Hao, D. Wu, Y. Ke, H. Gan, V. Laxmi, Z. Ouyang, F. Ouyang, Z. Wang, F. Liu, D. Qi, W. Zhang, *Adv. Funct. Mater.* **2021**, *31*, 2104143.
- [18] F. Wu, H. Xia, H. Sun, J. Zhang, F. Gong, Z. Wang, L. Chen, P. Wang, M. Long, X. Wu, J. Wang, W. Ren, X. Chen, W. Lu, W. Hu, *Adv. Funct. Mater.* **2019**, *29*, 1900314.
- [19] G. Jun, G. Wei, F. Dan, W. Huanting, Z. Dongyuan, *J. Am. Chem. Soc.* **2014**, *136*, 12265.
- [20] R. Zhuo, L. Zeng, H. Yuan, D. Wu, Y. Wang, Z. Shi, T. Xu, Y. Tian, X. Li, Y. H. Tsang, *Nano Res.* **2019**, *12*, 183.
- [21] T. Aichinger, P. M. Lenahan, B. R. Tuttle, D. Peters, *Appl. Phys. Lett.* **2012**, *100*, 112113.
- [22] F. Ahmed, Y. D. Kim, Z. Yang, P. He, E. Hwang, H. Yang, J. Hone, W. J. Yoo, *Nat. Commun.* **2018**, *9*, 3414.
- [23] D. Tan, X. Wang, W. Zhang, H. E. Lim, K. Shinokita, Y. Miyauchi, M. Maruyama, S. Okada, K. Matsuda, *Small* **2018**, *14*, 1704559.

- [24] C. Tan, H. Wang, X. Zhu, W. Gao, H. Li, J. Chen, G. Li, L. Chen, J. Xu, X. Hu, L. Li, T. Zhai, *ACS Appl. Mater. Interfaces* **2020**, *12*, 44934.
- [25] F. Wang, L. Yin, Z. X. Wang, K. Xu, F. M. Wang, T. A. Shifa, Y. Huang, C. Jiang, J. He, *Adv. Funct. Mater.* **2016**, *26*, 5499.
- [26] H. Shang, H. Chen, M. Dai, Y. Hu, F. Gao, H. Yang, B. Xu, S. Zhang, B. Tan, X. Zhang, P. Hu, *Nanoscale Horiz.* **2020**, *5*, 564.
- [27] Y. Chen, X. Wang, G. Wu, Z. Wang, H. Fang, T. Lin, S. Sun, H. Shen, W. Hu, J. Wang, J. Sun, X. Meng, J. Chu, *Small* **2018**, *14*, 1870038.
- [28] Y. Tang, Z. Wang, P. Wang, F. Wu, Y. Wang, Y. Chen, H. Wang, M. Peng, C. Shan, Z. Zhu, S. Qin, W. Hu, *Small* **2019**, *15*, 1805545.
- [29] M. Rahaman, C. Wagner, A. Mukherjee, A. Lopez-Rivera, S. Gemming, D. R. T. Zahn, *J. Phys.: Condens. Matter* **2019**, *31*, 114001.
- [30] T. Zheng, M. Yang, Y. Sun, L. Han, Y. Pan, Q. Zhao, Z. Zheng, N. Huo, W. Gao, J. Li, *J. Mater. Chem. C* **2022**, *10*, 7283.
- [31] H. Liu, X. Zhu, X. Sun, C. Zhu, W. Huang, X. Zhang, B. Zheng, Z. Zou, Z. Luo, X. Wang, D. Li, A. Pan, *ACS Nano* **2019**, *13*, 13573.
- [32] X. An, F. Liu, Y. J. Jung, S. Kar, *Nano Lett.* **2013**, *13*, 909.
- [33] M. Sun, D. Xie, Y. Sun, W. Li, T. Ren, *Nanotechnology* **2017**, *29*, 015203.
- [34] H. Yuan, X. Liu, F. Afshinmanesh, W. Li, G. Xu, J. Sun, B. Lian, A. G. Curto, G. Ye, Y. Hikita, Z. Shen, S.-C. Zhang, X. Chen, M. Brongersma, H. Y. Hwang, Y. Cui, *Nat. Nanotechnol.* **2015**, *10*, 707.
- [35] M. Amani, C. Tan, G. Zhang, C. Zhao, J. Bullock, X. Song, H. Kim, V. R. Shrestha, Y. Gao, K. B. Crozier, M. Scott, A. Javey, *ACS Nano* **2018**, *12*, 7253.
- [36] P. K. Venuthurumilli, P. D. Ye, X. Xu, *ACS Nano* **2018**, *12*, 4861.
- [37] F. Liu, S. Zheng, X. He, A. Chaturvedi, J. He, W. L. Chow, T. R. Mion, X. Wang, J. Zhou, Q. Fu, H. J. Fan, B. K. Tay, L. Song, R.-H. He, C. Kloc, P. M. Ajayan, Z. Liu, *Adv. Funct. Mater.* **2016**, *26*, 1169.
- [38] J. Lai, X. Liu, J. Ma, Q. Wang, K. Zhang, X. Ren, Y. Liu, Q. Gu, X. Zhuo, W. Lu, Y. Wu, Y. Li, J. Feng, S. Zhou, J.-H. Chen, D. Sun, *Adv. Mater.* **2018**, *30*, 1707152.
- [39] Y. Xin, X. Wang, Z. Chen, D. Weller, Y. Wang, L. Shi, X. Ma, C. Ding, W. Li, S. Guo, R. Liu, *ACS Appl. Mater. Interfaces* **2020**, *12*, 15406.
- [40] S. Zhao, J. Wu, K. Jin, H. Ding, T. Li, C. Wu, N. Pan, X. Wang, *Adv. Funct. Mater.* **2018**, *28*, 1802011.